Coupled Systems Mechanics, *Vol. 12, No. 5 (2023) 445-459*
https://doi.org/10.12989/csm.2023.12.5.445

Hybrid infrared-visible multiview correlation to study damage in a woven composite complex-shaped specimen

Andrija Zaplatić[1,2a], Zvonimir Tomičević*[1], Xuyang Chang[2b], Ivica Skozrit[1c], Stephane Roux[2d] and François Hild[2e]

[1]*Faculty of Mechanical Engineering and Naval Architecture, University of Zagreb, 10002 Zagreb, Croatia*
[2]*Université Paris-Saclay, CentraleSupélec, ENS Paris-Saclay, CNRS, LMPS, 91190 Gif-sur-Yvette, France*

(Received May 28, 2023, Revised July 10, 2023, Accepted July 29, 2023)

Abstract. In this study, a cyclic tensile test on a notched butterfly specimen made of woven glass fiber composite was performed on a modified Arcan fixture. During the mechanical test, the sample was monitored with a hybrid stereoscopic system comprised of two visible lights and one infrared camera. The visible light cameras were employed for kinematic measurements using a finite-element-based multiview correlation technique. A semi-hybrid correlation approach was followed, providing Lagrangian temperature fields of the Region of Interest. Due to the complex composite architecture and specimen shape, localized shearing was observed during the tensile loading. Furthermore, asymmetrical damage developed around the notches as revealed by localized strains and thermal hot spots.

Keywords: Arcan fixture; damage; full-field measurements; stereocorrelation; woven composite

1. Introduction

The growing industry standards impose strict requirements for modern materials. Nowadays, conventional engineering materials are substituted with fiber-reinforced polymer matrix composites, especially in high-tech engineering. Composites are lightweight materials, and their architecture can be finely tailored to specific loading conditions. By predicting the loading regimes of in-service conditions, their mass and manufacturing cost are then reduced. However, since composite architectures are complex (Vrgoč *et al.* 2021), extensive mechanical investigations are required for a comprehensive characterization of their degradation under different loading conditions.

Since composite materials are subjected to complex loading regimes during their operational

*Corresponding author, Associate Professor, E-mail: zvonimir.tomicevic@fsb.hr
[a]Ph.D. Student, E-mail: andrija.zaplatic@fsb.hr
[b]Post-doctoral Student, E-mail: xuyang.chang@ens-paris-saclay.fr
[c]Associate Professor, E-mail: ivica.skozrit@fsb.hr
[d]Research Professor, E-mail: Stephane.roux@ens-paris-saclay.fr
[e]Research Professor, E-mail: Francois.HILD@ens-paris-saclay.fr

http://www.techno-press.org/?journal=csm&subpage=8 ISSN: 2234-2184 (Print), 2234-2192 (Online)

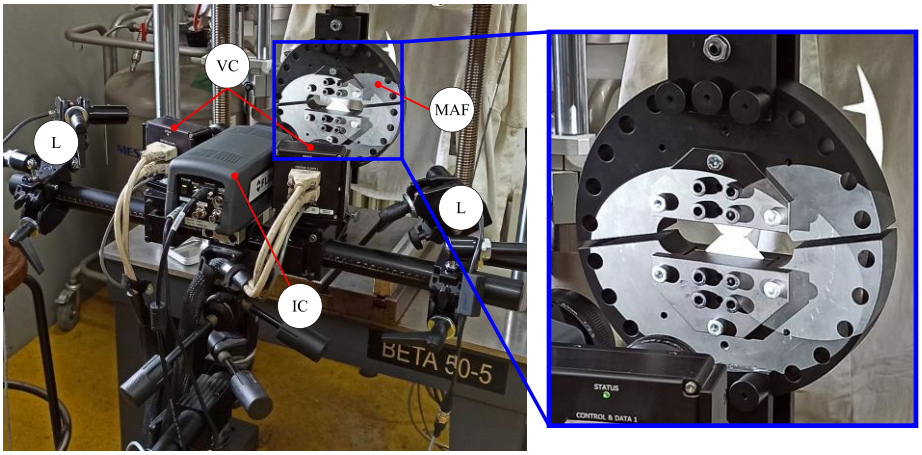

(a) (b)

Fig. 1 (a) Test setup with the modified Arcan fixture and cameras; see text for description of the labels (b) Modified Arcan fixture

time, it is necessary to carry out mechanical tests that simulate realistic working conditions. Tensile tests are the most common due to their simplicity and availability. To simulate different loading types, composite samples are cut at different angles (Vrgoč *et al.* 2021). However, using special loading devices, different loading types can be prescribed to the sample. The modified Arcan fixture or MAF (Zaplatić *et al.* 2022) is a well-established loading apparatus, which provides a wide range of loading types by simply rotating the device. The MAF was used for a variety of materials such as metals (Zaplatić *et al.* 2022, Zaplatić *et al.* 2023), composites (de Sousa Junior *et al.* 2017, Hao *et al.* 2019, Ud Din *et al.* 2020, Holmes *et al.* 2023), adhesive joints (Benelli *et al.* 2023), or wood (Xavier *et al.* 2009). However, advanced measurement protocols are necessary for the full-field characterization of Arcan samples.

The development of visible light cameras prompted the emergence of contactless full-field measurement methods where Digital Image Correlation (DIC) stands out as the most used tool (Sutton *et al.* 2009). In its fundamental form, DIC discretizes the observed region of interest (ROI) into a number of subsets (or facets) and measures the displacements of the center of each facet independently. The drawback of such approaches is the independently measured kinematics, which results in discontinuities, thus requiring additional post-processing interpolation/smoothing. This step can be avoided by using finite element (FE) based DIC, which assumes the continuity of the displacement field over the entire ROI (Hild and Roux 2012). For complex sample geometries, Multiview Correlation or MC (aka stereocorrelation) may be used. MC may also exploit FE meshes (Berny *et al.* 2021). Furthermore, the optical setup can be enriched by adding an infrared camera in so-called hybrid environments (Charbal *et al.* 2016, Wang *et al.* 2020). With hybrid setups, displacements and temperatures are measured simultaneously using hybrid multiview correlation (HMC) algorithms (Dufour *et al.* 2015, Charbal *et al.* 2016, Wang *et al.* 2020).

The aim of this paper is to characterize the response of a woven glass fiber sample under tensile loading. The MAF is used to load the butterfly specimen. A hybrid stereoscopic setup consisting of two visible light and one infrared cameras is employed. FE-based MC is used for displacement and strain measurements. Moreover, a semi-hybrid algorithm is implemented in order to obtain Lagrangian temperature fields using the measured displacement fields.

Table 1 Hardware parameters of the hybrid system

Cameras	2×Dalsa Falcon 4M60	Flir A6751
Definition	2358×1728 px	640×512 px
Digitization	8-bits	16-bits
Lens	Titanar 50 mm	Flir 50 mm
Distance ring	7 mm	6.35 mm
Aperture	f/5.6	-
Stereo-angle	25°	0°
Stand-off distance	260 mm	265 mm
Camera distance	88 mm	-
Image acquisition rate	1 fps	1 fps
Patterning technique	B/W paint	-

2. Experimental investigation

In this research, a cyclic tensile test was carried out with the MAF. The 3-mm thick butterfly specimen was made of woven glass fibers infused with a vinylester resin. The yarns were oriented at 0°/90° along the loading direction. Two notches were cut with a band saw in the central gauge area of the sample. The length of the notches was approximately 2 mm long and 1 mm wide. The speckle pattern on the sample was created by spraying a thin layer of white paint on the surface, and then fine black speckles were applied using a paintbrush. The speckle pattern was not visible in the IR spectrum, hence uniform emissivity ($\varepsilon = 0.96$ (Leistner *et al.* 2019)) was assumed over the observed Region of Interest (ROI). The sample was loaded with a 0.24 mm/min rate in displacement control mode. The experimental and optical setups are shown in Fig. 1. The sample surface was monitored by a stereo-optical camera pair (VL) and one infrared camera (IC) with two light sources (L). In this work, only visible light cameras were used for displacement measurements. The hardware parameters of the optical setup are listed in Table 1.

3. Multiview calibration and correlation

In this section, the FE-based MC algorithm is presented. It is based on the pinhole camera model, which allows any 3D point to be projected onto 2D image planes of each camera *c*

$$s^c \cdot \begin{Bmatrix} x^c \\ y^c \\ 1 \end{Bmatrix} = \left[\mathbf{\Pi}^c \right] \begin{Bmatrix} X \\ Y \\ Z \\ 1 \end{Bmatrix}, \tag{1}$$

where $[\mathbf{\Pi}^c]$ is the projection matrix, s^c the scale factor, x^c and y^c the projected image coordinates of the FE nodal coordinates *X, Y* and *Z*. The projection matrix $[\mathbf{\Pi}^c]$ is calculated by multiplying the intrinsic $[\mathbf{K}^c]$ and extrinsic $[\mathbf{T}^c]$ matrices

$$\left[\mathbf{\Pi}^c\right]=\left[\mathbf{K}^c\right]\left[\mathbf{T}^c\right]=\begin{bmatrix} f_x & \xi & c_x \\ 0 & f_y & c_y \\ 0 & 0 & 1 \end{bmatrix}\begin{bmatrix} r_{11} & r_{12} & r_{13} & t_x \\ r_{21} & r_{22} & r_{23} & t_y \\ r_{31} & r_{32} & r_{33} & t_z \end{bmatrix}. \tag{2}$$

where f_x and f_y are the horizontal and vertical scale factors expressed in pixels, c_x and c_y the positions of the optical center, and ξ is the skew angle which is often disregarded since the horizontal and vertical scale factors are similar. The parameters r_{ij} in the extrinsic matrix $[\mathbf{T}^c]$ refer to three Euler angles ψ, φ and θ and their combinations. Finally, the last three parameters of the extrinsic matrix $[\mathbf{T}^c]$ are three translations t_x, t_y and t_z in x, y and z directions, respectively. During the calibration procedure, the extrinsic and intrinsic parameters are determined for each camera to construct the projection matrices $[\mathbf{\Pi}^c]$.

3.1 Camera calibration procedure

The calibration procedure was initialized by *Point and Perspective* (PnP) solutions (Lepetit *et al.* 2009) solutions to obtain initial guesses of the extrinsic and intrinsic parameters from which the initial projection matrices $[\mathbf{\Pi}^c]$ are constructed for each camera c. At least 6 points are chosen on the FE mesh ($\mathbf{X}$), and their respective positions in the images are selected ($\boldsymbol{x}^c$). For calibration, gray level conservation is assumed such that the pictures captured by the left $f^1(\boldsymbol{x}^1)$ and right $f^2(\boldsymbol{x}^2)$ cameras (where $\boldsymbol{x}^c = (x^c, y^c)$ and c=1 or 2) satisfy

$$f^1\left(\boldsymbol{x}^1\right)= f^2\left(\boldsymbol{x}^2\right) \tag{3}$$

Eq. (3) is only valid if the calibration parameters are properly determined without any acquisition noise. Therefore, a global formulation is performed where the Sum of Squared Differences (SSD)

$$\rho^2\left(\{\mathbf{P}\}\right)=\left\| f^1\left(\boldsymbol{x}^1\left(\mathbf{X},\left[\mathbf{\Pi}^1\right]\right)\right)- f^2\left(\boldsymbol{x}^2\left(\mathbf{X},\left[\mathbf{\Pi}^2\right]\right)\right)\right\|^2 \tag{4}$$

is minimized over the chosen ROI where ρ denotes the calibration residuals and $\{\mathbf{P}\}$ collects the intrinsic and extrinsic parameters of the two cameras. For this integrated approach, the intrinsic and extrinsic parameters are first calibrated, and from which the projection matrices $[\mathbf{\Pi}^{1,2}]$ are then obtained. The sensitivity fields with respect to each parameter are computed via finite differences. The small parameter variations lead to pseudo-displacement fields in the 2D camera planes for each 3D point from $\boldsymbol{x}^c$ to $\boldsymbol{x}^c + \delta\boldsymbol{x}^c$ from which the sensitivity field for each camera is expressed as

$$\mathbf{S}_\mathbf{P}^c = \frac{\delta \boldsymbol{x}^c}{\delta \mathbf{P}^c} \tag{5}$$

which is a 2D vector field defined at each evaluation point $\mathbf{X}$. In the calibration procedure, the intrinsic and extrinsic parameters are progressively updated to minimize the cost function (4) via Gauss-Newton iterations. After computing the sensitivity fields, the Hessian $[\mathbf{H}^c]$ for each camera is computed as

$$\left[\mathbf{H}^c\right]=\sum_{ROI}\left[\nabla f^c\left(\boldsymbol{x}^c\left(\mathbf{X},\left[\mathbf{\Pi}^c\right]\right)\right)\cdot\mathbf{S}_\mathbf{P}^c\right]^\mathrm{T}\left[\nabla f^c\left(\boldsymbol{x}^c\left(\mathbf{X},\left[\mathbf{\Pi}^c\right]\right)\right)\cdot\mathbf{S}_\mathbf{P}^c\right] \tag{6}$$

All camera-wise Hessian matrices are gathered in the global Hessian matrix [**C**]

$$\left[\mathbf{C}\right]=\begin{bmatrix}\left[\mathbf{H}^1\right] & 0\\ 0 & \left[\mathbf{H}^2\right]\end{bmatrix} \tag{7}$$

Next, the camera parameter-based second member $\{\mathbf{b}^c\}$ is expressed as

$$\begin{aligned}\left\{\mathbf{b}^1\right\}&=\sum_{ROI}\left[\mathbf{S}_\mathbf{P}^1\cdot\nabla f^1\left(\boldsymbol{x}^1\right)\right]^T\cdot\left(f^1\left(\boldsymbol{x}^1\left(\mathbf{X},\left[\boldsymbol{\Pi}^1\right]\right)\right)-f^2\left(\boldsymbol{x}^2\left(\mathbf{X},\left[\boldsymbol{\Pi}^2\right]\right)\right)\right)\\ \left\{\mathbf{b}^2\right\}&=\sum_{ROI}\left[\mathbf{S}_\mathbf{P}^2\cdot\nabla f^2\left(\boldsymbol{x}^2\right)\right]^T\cdot\left(f^2\left(\boldsymbol{x}^2\left(\mathbf{X},\left[\boldsymbol{\Pi}^2\right]\right)\right)-f^1\left(\boldsymbol{x}^1\left(\mathbf{X},\left[\boldsymbol{\Pi}^1\right]\right)\right)\right)\end{aligned} \tag{8}$$

and are gathered in the global second member

$$\left\{\mathbf{B}\right\}=\begin{Bmatrix}\left\{\mathbf{b}^1\right\}\\ \left\{\mathbf{b}^2\right\}\end{Bmatrix} \tag{9}$$

At each iteration step the corrections to the sought parameters for each camera are calculated

$$\left\{\delta\mathbf{P}\right\}=\left[\mathbf{C}\right]^{-1}\left\{\mathbf{B}\right\} \tag{10}$$

until the convergence criterion over the stationarity of the residuals, expressed in gray levels, is satisfied

$$\Delta\rho=\rho^n-\rho^{n-1}<10^{-5} \tag{11}$$

where n is the number of the current iteration.

3.2 Kinematic measurements

After calibrating the cameras, the nodal-wise kinematic field **U**(**X**) is measured at any given time t. The new SSD cost function considers the reference images f^c and corrected deformed image $\tilde{g}^c(t)$ at time t for each respective camera

$$\mathbf{U}(\mathbf{X},t)=\min\sum_{1}^{c=Nc}\sum_{ROI}\left(\tilde{g}^c_{\mathbf{U}(\mathbf{X},t)}\left(\boldsymbol{x}^c\left(\mathbf{X},\left[\boldsymbol{\Pi}^c\right]\right),t\right)-f^c\left(\boldsymbol{x}^c\left(\mathbf{X},\left[\boldsymbol{\Pi}^c\right]\right)\right)\right)^2 \tag{12}$$

where $\tilde{g}^c_{\boldsymbol{U}(\boldsymbol{X},t)}(x^c(\boldsymbol{X},[\boldsymbol{\Pi}^c]),t)$ represents the deformed image acquired by camera c at time t corrected by the displacement field $\boldsymbol{U}(\boldsymbol{X},t)$ and N_c the number of cameras. The regularity of the kinematic field $\boldsymbol{U}(\boldsymbol{X},t)$ in space, is ensured using a set of spatial shape functions $\boldsymbol{\Phi}$(**X**)

$$\mathbf{U}\left(\mathbf{X},t\right)=\sum_{1}^{i=N_{DOF}}u_i\left(t\right)\boldsymbol{\Phi}_i\left(\mathbf{X}\right) \tag{13}$$

where N_{DOF} is the number of degrees of freedom, u_i the nodal displacements determined at each step t. In the present case, three-noded (T3) elements were considered (Berny *et al.* 2021). An iterative Gauss-Newton scheme was employed for the FE-based MC procedure. Therefore, the Hessian matrix [$\mathbf{H}_U$] and second member vector {$\mathbf{B}_U$} need to be computed

$$\left[\mathbf{H}_{\mathrm{U}}\right]=\sum_{1}^{c=N_c}\sum_{ROI}\left(\boldsymbol{\Phi}(\mathbf{X})\cdot\frac{\partial \boldsymbol{x}^c}{\partial \mathbf{X}}\cdot\nabla f^c\left(\boldsymbol{x}^c\left(\mathbf{X},\left[\boldsymbol{\Pi}^c\right]\right)\right)\right)^{\mathrm{T}}\left(\boldsymbol{\Phi}(\mathbf{X})\cdot\frac{\partial \boldsymbol{x}^c}{\partial \mathbf{X}}\cdot\nabla f^c\left(\boldsymbol{x}^c\left(\mathbf{X},\left[\boldsymbol{\Pi}^c\right]\right)\right)\right) \tag{14}$$

and

$$\left\{\mathbf{B}_{\mathrm{U}}\right\}=\sum_{1}^{c=N_c}\sum_{ROI}\left(\boldsymbol{\Phi}(\mathbf{X})\cdot\frac{\partial \boldsymbol{x}^c}{\partial \mathbf{X}}\cdot\nabla f^c\left(\boldsymbol{x}^c\left(\mathbf{X},\left[\boldsymbol{\Pi}^c\right]\right)\right)\right)^{\mathrm{T}}\cdot\left(\tilde{g}^c_{\mathbf{U}(\mathbf{X},t)}\left(\boldsymbol{x}^c\left(\mathbf{X},\left[\boldsymbol{\Pi}^c\right]\right),t\right)-f^c\left(\boldsymbol{x}^c\left(\mathbf{X},\left[\boldsymbol{\Pi}^c\right]\right)\right)\right) \tag{15}$$

where $\frac{\partial \boldsymbol{x}^c}{\partial \mathbf{X}}$ is the displacement sensitivity. The nodal displacement amplitude corrections are calculated

$$\left\{\delta \boldsymbol{u}\right\}=\left[\mathbf{H}_{\mathrm{U}}\right]^{-1}\left\{\mathbf{B}_{\mathrm{U}}\right\} \tag{16}$$

and the nodal displacement vector is updated

$$\left\{\boldsymbol{u}(t)\right\}=\left\{\boldsymbol{u}(t)\right\}+\left\{\delta \boldsymbol{u}(t)\right\}. \tag{17}$$

The camera-wise gray-level residuals $\boldsymbol{\varphi}^{\boldsymbol{c}}$ are computed for each evaluation point

$$\varphi^c\left(\boldsymbol{x}^c\right)=\tilde{g}^c_{\mathbf{U}(\mathbf{X},t)}\left(\boldsymbol{x}^c\left(\mathbf{X},\left[\boldsymbol{\Pi}^c\right]\right),t\right)-f^c\left(\boldsymbol{x}^c\left(\mathbf{X},\left[\boldsymbol{\Pi}^c\right]\right)\right) \tag{18}$$

3.3 IR camera

It should be noted that, since the speckle pattern was not visible in IR images, the IR camera could not be calibrated with the approach presented in Section 3.1. Hence only the PnP solution of the projection matrix [$\boldsymbol{\Pi}^3$] was used. Furthermore, no prior IR camera calibration for the tested sample surface was performed and a uniform emissivity $\varepsilon = 0.96$ was assumed over the entire ROI. The measured displacements $\boldsymbol{U}(\boldsymbol{X},t)$ need to be transformed from the FE mesh perspective to the camera plane. The nodal displacements in the IR camera plane $\boldsymbol{u}^{IR}$ are defined

$$\mathbf{u}^{IR}(t)=\mathbf{x}_g^{IR}-\mathbf{x}_f^{IR}(t) \tag{19}$$

where $\boldsymbol{x}_f^{IR}$ is the position of any projected FE node onto the IR camera plane in the reference configuration, and $\boldsymbol{x}_g^{IR}(t)$ that in the deformed configuration. The next step was to determine the projector matrix [**p**], which is used to interpolate nodal values to pixel positions. With the known nodal displacements, it is possible to compute the displacement fields for any pixel position

$$\begin{aligned}\left\{\mathbf{u}_x^{px}(t)\right\}&=\left[\mathbf{p}\right]\cdot\left\{\mathbf{u}_x^{IR}(t)\right\}\\ \left\{\mathbf{u}_y^{px}(t)\right\}&=\left[\mathbf{p}\right]\cdot\left\{\mathbf{u}_y^{IR}(t)\right\}\end{aligned} \tag{20}$$

where $\boldsymbol{u}^{px}$ are the pixel-wise displacements of the ROI. Finally, the IR images were then corrected using the pixel-wise displacements

$$T(\mathbf{x},t)=g^{IR}\left(\mathbf{x}+\mathbf{u}^{px}(\mathbf{x},t),t\right) \tag{21}$$

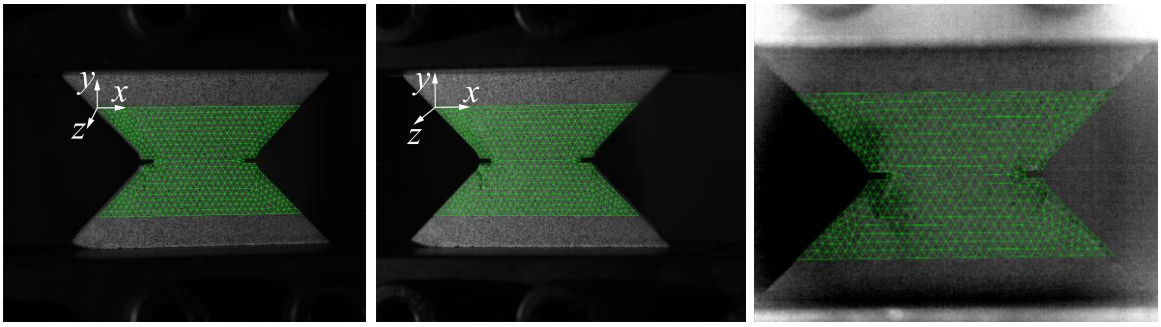

(a) (b) (c)

Fig. 2 Projected 3D mesh with the calibrated projection matrices [$\mathbf{\Pi}^c$] on the image plane of the first (a) and second (b) visible light cameras as well as the IR camera (c)

Table 2 Hybrid multiview analysis parameters

DIC software	Correli 3.0			
Image filtering	None			
Average element length	0.7 mm			
Shape functions	Linear (T3 elements)			
Matching criterion	Sum of squared differences			-
Temperature noise floor	-			0.05°C
Displacement noise floor	U_x	U_y	U_z	-
	0.3 μm	0.4 μm	2 μm	
Strain noise floor	ε_x	ε_y	γ_{xy}	
	5×10^{-4}	6×10^{-4}	4×10^{-4}	

where $T(\boldsymbol{x}, t)$ is the pixel-wise Lagrangian temperature field of the ROI. Since the displacement fields were obtained via FE-based MC performed with images acquired with visible light cameras, it is a semi-hybrid procedure (in contrast with a full hybrid that would include the IR images in the determination of the displacement field (Wang *et al.* 2020).

4. Experimental results

In this section, the multimodal results are discussed. Before the experiment, a set of 10 images was captured in the unloaded state for each camera, which were used for the calculation of measurements uncertainties (Table 2). A single pair of visible light images was used for the full calibration of the projection matrices. The geometry of the sample and its relation to the MAF was known a priori. Hence, characteristic points related to the sample and MAF were used to initialize the calibration procedure. The final projection matrices [$\mathbf{\Pi}^c$] provided good results for the 3D mesh, once projected onto each image plane of the three cameras (Fig. 2). Moreover, a calibration object may be desirable given the planar shape of the sample.

The tensile test consisted of eight loading/unloading cycles. In Fig. 3, the mean net section stress is displayed, which was calculated by dividing the measured force with the initial ligament

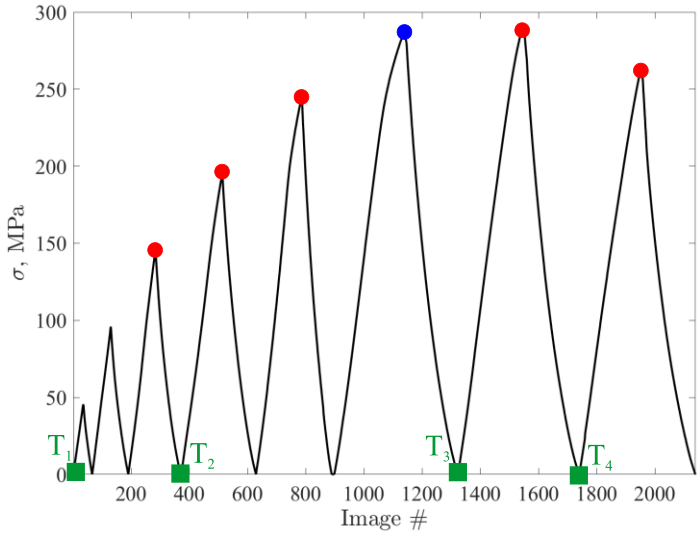

Fig. 3 Loading history of the tensile test. Five characteristic points are outlined by red circles for which kinematic and temperature measurements are reported hereafter. The chosen net section stress levels are 145, 196, 245, 289 and 262 MPa. The blue point denotes 99% of the ultimate tensile strength (289 MPa). The results for this level are not displayed since they were very close to the next one. The green rectangles denote the first image of each loading cycle between CT scans

(a) (b) (c)

Fig. 4 Measured displacement fields expressed in mm for the first cycle peak (145 MPa). Components U_x (a), U_y (b) and U_z (c)

area. The cycles were defined *a priori* by conducting a monotonic tensile test with the same experimental setup and same material. The sample was removed five times from the MAF during the test in order to access any microstructural changes via X-ray computed tomography (CT) (Bartulović *et al.* 2022). The effects of unmounting and remounting of the sample are discussed hereafter. The presented IR images are corrected by subtracting the current temperature field T with the first image of the corresponding loading cycle (Fig. 3). This operation is possible thanks to the fact that Lagrangian fields were obtained.

The first results are for the images captured for the peak of the elastic regime of the material. The displacements for a stress level of 145 MPa are displayed in Fig. 4. The tensile loading axis corresponds to the y-direction (vertical direction in Fig. 2). The largest displacements are reported for the top left and right parts of the ROI. This is due to the geometry of the sample where the central part exhibited higher stiffness than the peripheral zones of the ROI. Displacement gradients are detected in a narrow zone around the notches as well as along vertical lines emanating from the notches. These phenomena are also observed in Fig. 5 and Fig. 6.

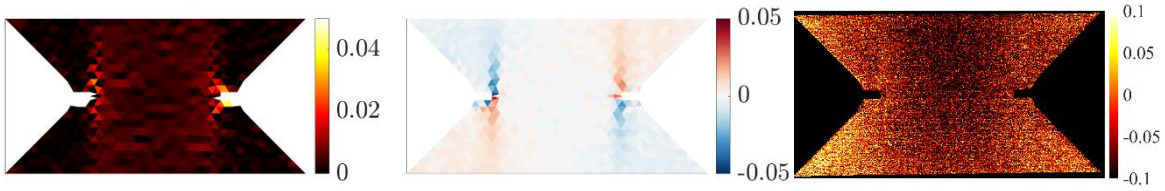

(a) (b) (c)

Fig. 5 Measured strain and temperature fields for the first cycle peak (145 MPa). (a) ε_{yy}, (b) ε_{xy} and (c) ΔT=T-T_1 (in °C)

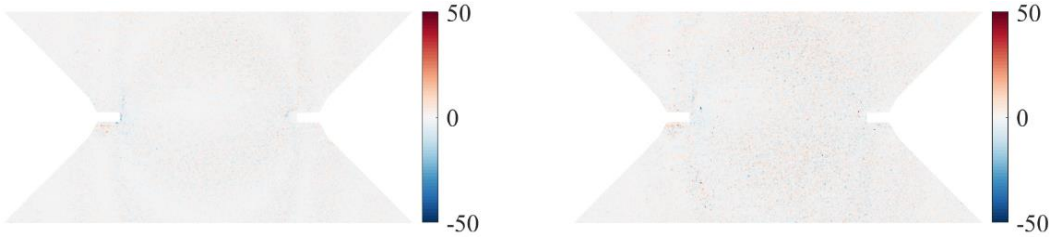

(a) (b)

Fig. 6 Gray level residuals for the first cycle peak (145 MPa) for the first (a) and second (b) cameras

(a) (b) (c)

Fig. 7 Measured displacement fields expressed in mm for the second cycle peak (196 MPa). Components U_x (a), U_y (b) and U_z (c)

The highest strain levels (Fig. 5) are concentrated in small zones around the notches. On both longitudinal (Fig. 5(a)) and shear (Fig. 5(b)) strain fields, two bands oriented along the loading direction are observed. The strain levels on both fields are of the same order of magnitude. Furthermore, the temperature field (Fig. 5(c)) reveals slight decreases in temperature in the center of the sample between the notches, which correspond to thermoelastic effects (Crupi *et al.* 2015).

The correlation residuals (Fig. 6) for this stage between the reference and corrected deformed images reveal very small differences, which may be safely attributed to acquisition noise thereby indicating full convergence of the FE-based MC algorithm.

The second set of results (Figs. 7 and 8) correspond to early onset of mechanical nonlinearity. Increased out-of-plane z displacements is noted (Fig. 7(c)). The rise of these displacements was caused by the first unmounting and remounting of the sample. These perturbations caused rigid body motions, which do not influence the strain fields. The displacements in the y-direction indicate high gradients due to shear bands.

Strained bands are observed on both longitudinal (Fig. 8(a)) and shear (Fig. 8(b)) strain fields. Higher strain levels are reported for the left notch. The temperature field (Fig. 8(c)) still reveals thermoelastic effects in in the entire area between the notches.

(a) (b) (c)

Fig. 8 Measured strain and temperature fields for the second cycle peak (196 MPa). (a) ε_{yy}, (b) ε_{xy} and (c) ΔT=T-T_2 (in °C)

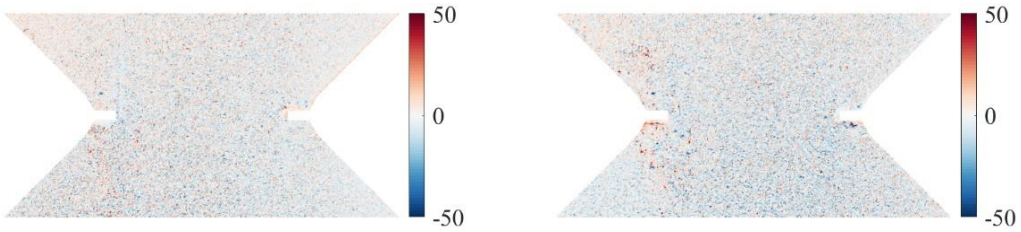

(a) (b)

Fig. 9 Gray level residuals for the second cycle peak (196 MPa) for the first (a) and second (b) cameras

(a) (b) (c)

Fig. 10 Measured displacement fields expressed in mm for the third cycle peak (245 MPa). Components U_x (a), U_y (b) and U_z (c)

The correlation residual levels (Fig. 9) increased overall. The main cause is attributed to changes in brightness and contrast (BC) compared to the reference states, which is seen in the residual levels between the left and right images. It is especially apparent for the second camera. Such a uniform change may result from a rotation of the sample surface with regards to the lighting sources, due to non-Lambertian surface reflectivity/diffusivity. The highest residuals occurred on the left peripheral part of the sample where BC changed the most for both cameras.

Increasing the applied stress by 50 MPa, the displacement fields in the *y*-direction (Fig. 10(b)) experienced the largest change. The displacements in the *y*-direction display much higher gradients due to shear than in Fig. 7(b). Moreover, the displacement fields in *x* and *z*-directions (Fig. 10(a), (c)) experienced very small changes. The high gradients observed in the *x*-direction for U_y displacement field are not observed in the *x* and *z* displacement fields.

The gradients observed in the previous figure have a direct signature in the strain fields shown in Fig. 11. Strain (shear) bands are visible in both longitudinal (Fig. 11(a)) and shear (Fig. 11(b)) strain fields. They are more pronounced than for the previous load level. Both longitudinal and shear strains have similar levels. Increased temperatures are noted in the lower right corner of the ROI (see Fig. 11(c)) and the same localization is present in the strain fields, but not in the residual

(a) (b) (c)

Fig. 11 Measured strain and temperature fields for the third cycle peak (245 MPa). (a) ε_{yy}, (b) ε_{xy} and (c) ΔT=T-T_2 (in °C)

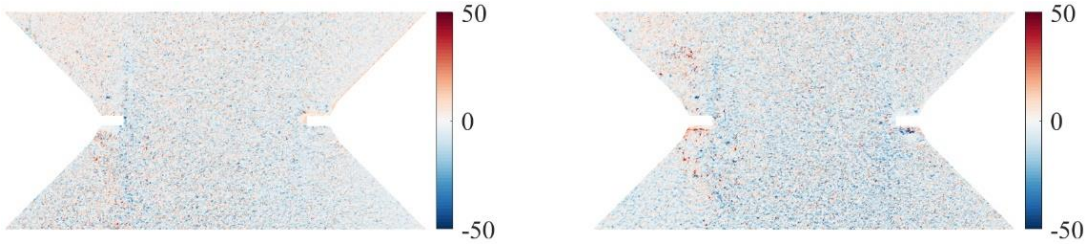

(a) (b)

Fig. 12 Gray level residuals for the third cycle peak (245 MPa) for the first (a) and second (b) cameras

(a) (b) (c)

Fig. 13 Measured displacement fields expressed in mm for the fourth cycle peak (289 MPa). Components U_x (a), U_y (b) and U_z (c)

fields (Fig. 12). Since the increase temperature is minimal, it is attributed to artefactual heating originating from the testing machine and lighting.

The gray level residual fields (Fig. 12) were similar to the previous cycle (Fig. 9), thereby indicating that the BC conditions did not change much during one further unmounting/remounting step. However, increased residuals are noted perpendicular to the left notch, oriented along the loading direction. This location matches that of the shear strain bands. Moreover, below the right hand side notch, the increased residuals coincide with the highest strains (Fig. 11).

The next step corresponds to the ultimate tensile load level tested to investigate whether any damage initiated on the monitored surface. Before this cycle, the sample was removed and mounted again. Rigid body motions are observed from the displacement fields in x and z-directions (Fig. 13(a, c)). High gradients are detected in the displacement field in the y-direction (Fig. 13(b)) between the center and peripheral parts of the sample.

Several shear bands are observed in the strain fields shown in Fig. 14. As seen from the high gradients in Fig. 13, increased strains occurred around the notches. The highest strain levels were reached above the left notch where also a faint variation in temperature is observed indicating that the strain levels were reached earlier, leading to lower temperature and a more diffuse signature.

(a) (b) (c)

Fig. 14 Measured strain and temperature fields for the fourth cycle peak (289 MPa). (a) ε_{yy}, (b) ε_{xy} and (c) ΔT=T-T_3 (in °C)

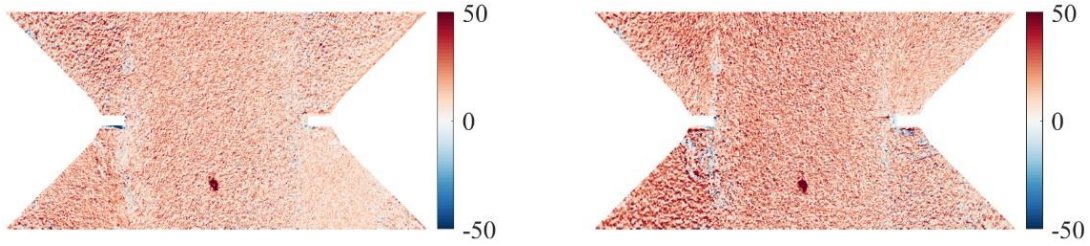

(a) (b)

Fig. 15 Gray level residuals for the fourth cycle peak (289 MPa) for the first (a) and second (b) cameras

(a) (b) (c)

Fig. 16 Measured displacement fields expressed in mm for the fifth cycle peak (262 MPa). Components U_x (a), U_y (b) and U_z (c)

Above the right notch, increased strain levels are also present. This is also observable in the IR image (Fig. 14(c)) where increased changes in temperature are present due to energy dissipation during damage initiation.

The correlation residuals (Fig. 15) reveal changes in BC conditions as for the previously discussed results. For the second camera, the overall residuals are higher than for the first one. Increased residuals are located around the notches. On the notch roots, small areas with higher levels indicate the presence of initiated cracks as was observed in the strain and displacement fields. Furthermore, below the right notch, higher residuals correspond to the shear band that propagated on its edge. A spot with high residuals is also present in the lower central part of the ROI. This was caused by a damaged speckle pattern, which was not related to the loading of the sample but due to its mounting/unmounting.

For the final loading step, the maximum load was lower than the previous one, thus indicating that damage further developed in the sample. Severe gradients are detected in the displacement fields (Fig. 16), especially around the right notch root from which another strain band emanated (Fig. 17). The sample was removed from the testing machine before this last cycle, which caused rigid body motions seen in the *y* and *z*-directions (Fig. 17(a-c)).

(a) (b) (c)

Fig. 17 Measured strain and temperature fields for the first cycle peak (262 MPa). (a) ε_{yy}, (b) ε_{xy} and (c) ΔT=T-T_4 (in °C)

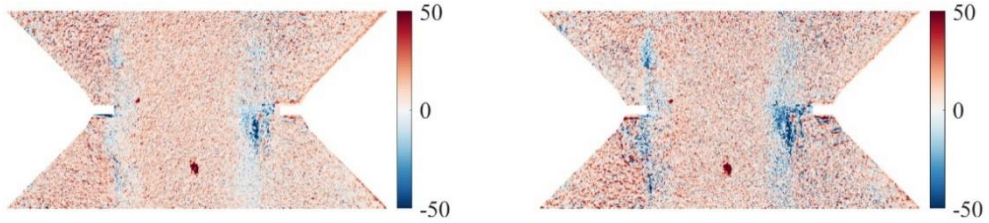

(a) (b)

Fig. 18 Gray level residuals for the fifth cycle peak (262 MPa) for the first (a) and second (b) cameras

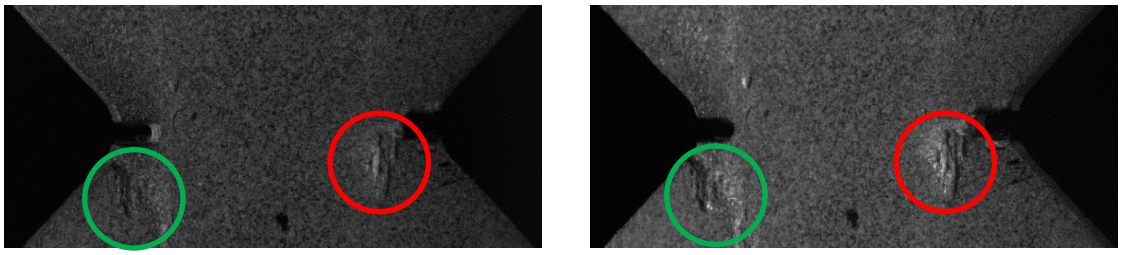

(a) (b)

Fig. 19 Images of the damaged sample acquired by the first (a) and second (b) visible light cameras at the fifth cycle peak. The red circle indicates surface damage. The green circle indicates the surface deformity, which originates from the manufacturing process

The strain fields reveal several shear bands, with two in the vicinity of the right notch where severe damage occurred. In all strain fields (Fig. 17 (a, b)), the bands around the right notch are visible. Moreover, higher changes in temperature are observed in that area, highlighting energy dissipation due to damage. A change in temperature also occurred around the left notch in the same location as high strain levels are reported.

The correlation residuals (Fig. 18) also reveal high levels in the same locations as the strain bands evidenced in the displacement and strain fields. The highest residuals are located under the right notch. Damage also occurred above the left notch, which is clearer for the second camera.

The gray level residuals are compared to the raw images (Fig. 19). The increased residuals correspond to damage observed on the images. Due to differences in BC between images, the residual fields are also slightly different. Moreover, the peripheral areas of the ROI exhibit increased residuals for both cameras. The underlying damage caused the speckled surface to break, hence the FE-based MC algorithm could not converge between the reference and the deformed image since the gray level conservation was violated. From Fig. 19, it is confirmed that damage

was more extensive in the vicinity of the right notch (Fig. 19 red circle).

5. Conclusions

In this study, a cyclic tensile test was performed on a notched glass fiber woven composite with an MAF. A hybrid optical setup with two visible light and one infrared cameras was used to monitor the surface motion of the sample. An FE-based multiview correlation algorithm was employed to measure displacement, strain and temperature fields. The main results of this work are:

- A semi-hybrid multiview procedure was implemented in which Lagrangian temperature fields could be reported over the investigated ROI *in addition to* displacement and strain fields using the exact same spatial coordinates.
- Although unidirectional tensile load was applied on the sample, shear strain bands emanated from the two notches because of the sample geometry and the underlying woven architecture.
- Damage initiated and developed asymmetrically around both notches, which indicates a significant influence of the woven fabric.

Improvements to the experimental setup could enable for a complete multiview and hybrid analysis to be performed. Last, brightness and contrast corrections could be implemented.

Acknowledgments

This work was performed within the FULLINSPECT project supported by the Croatian Science Foundation (UIP-2019-04-5460 Grant). AZ was also supported through the Incoming International Scholarship Program of ENS Paris-Saclay. This work was also partially supported by the European Union through the European Regional Development Fund, Operational Programme "Competitiveness and Cohesion" 2014-2020 of the Republic of Croatia, project "Improvement of high-efficiency welding technology" (ImproWE, KK.01.1.1.07.0076).

References

Bartulović, A., Tomičević, Z., Bubalo, A. and Hild, F. (2022), "Assessment of DVC measurement uncertainty on GFRPs with various fiber architectures", *Coupled Syst. Mech.*, **11**(1), 15-32. https://doi.org/10.12989/csm.2022.11.1.015.

Benelli, A., Ciardiello, R., Boursier Niutta, C. and Goglio, L. (2023), "Experimental and numerical characterization of adhesive joints with composite substrates by means of the Arcan test", *Int. J. Adhes. Adhesiv.*, **122**, 103321. https://doi.org/10.1016/j.ijadhadh.2022.103321.

Berny, M., Archer, T., Beauchêne, P., Mavel, A. and Hild, F. (2021), "Displacement uncertainty quantifications in T3-stereocorrelation", *Exp. Mech.*, **61**(5), 771-790. https://doi.org/10.1007/s11340-021-00690-0.

Berny, M., Archer, T., Hild, F., Mavel, A., Beauchêne, P., Herb, V. and Lacombe, B. (2019), "On performing spatiotemporal stereocorrelation at very high temperatures", *Conference Proceedings of the Society for Experimental Mechanics Series*, **12**, 181-183. https://doi.org/10.1007/978-3-319-97481-1_24.

Berny, M., Archer, T., Mavel, A., Beauchêne, P., Roux, S. and Hild, F. (2018), "On the analysis of heat haze effects with spacetime DIC", *Opt. Laser. Eng.*, **111**, 135-153. https://doi.org/10.1016/j.optlaseng.2018.06.004.

Charbal, A., Dufour, J.E., Hild, F., Poncelet, M., Vincent, L. and Roux, S. (2016), "Hybrid stereocorrelation using infrared and visible light cameras", *Exp. Mech.*, **56**(5), 845-860. https://doi.org/10.1007/s11340-016-0127-4.

Crupi, V., Guglielmino, E., Risitano, G. and Tavilla, F. (2015), "Experimental analyses of SFRP material under static and fatigue loading by means of thermographic and DIC techniques", *Compos. Part B: Eng.*, **77**, 268-277. https://doi.org/10.1016/j.compositesb.2015.03.052.

de Sousa Junior, R.R., Gouveia, J.R., Ito, N.M. and dos Santos, D.J. (2017), "Failure prediction of hybrid composite using Arcan's device and Drucker-Prager model", *Polym. Test.*, **58**, 256-261. https://doi.org/10.1016/j.polymertesting.2017.01.001.

Dufour, J.E., Hild, F. and Roux, S. (2015), "Shape, displacement and mechanical properties from isogeometric multiview stereocorrelation", *J. Strain Anal. Eng. Des.*, **50**(7), 470-487. https://doi.org/10.1177/0309324715592530ï.

Hao, P., Din, I.U. and Panier, S. (2019), "Development of modified Arcan fixture for biaxial loading response of fiber-reinforced composites", *Polym. Test.*, **80**, 106148. https://doi.org/10.1016/j.polymertesting.2019.106148.

Hild, F. and Roux, S. (2012), "Comparison of local and global approaches to digital image correlation", *Exp. Mech.*, **52**(9), 1503-1519. https://doi.org/10.1007/s11340-012-9603-7.

Holmes, J., Sommacal, S., Das, R., Stachurski, Z. and Compston, P. (2023), "Digital image and volume correlation for deformation and damage characterisation of fibre-reinforced composites: A review", *Compos. Struct.*, **315**, 116994. https://doi.org/10.1016/j.compstruct.2023.116994.

Leistner, C., Löffelholz, M. and Hartmann, S. (2019), "Model validation of polymer curing processes using thermography", *Polym. Test.*, **77**, 105893. https://doi.org/10.1016/j.polymertesting.2019.05.009.

Lepetit, V., Moreno-Noguer, F. and Fua, P. (2009), "EPnP: An accurate O(n) solution to the PnP problem", *Int. J. Comput. Vision*, **81**(2), 155-166. https://doi.org/10.1007/s11263-008-0152-6.

Sutton, M.A., Orteu, J.J. and Schreier, H. (2009), *Image Correlation for Shape, Motion and Deformation Measurements: Basic Concepts, Theory and Applications*, Springer Science & Business Media.

Ud Din, I., Hao, P., Panier, S., Khan, K.A., Aamir, M., Franz, G. and Akhtar, K. (2020), "Design of a new arcan fixture for in-plane pure shear and combined normal/shear stress characterization of fiber reinforced polymer composites", *Exp. Techniq.*, **44**(2), 231-240. https://doi.org/10.1007/s40799-019-00353-9.

Vrgoč, A., Tomičević, Z., Smaniotto, B. and Hild, F. (2021), "Damage characterization in fiber reinforced polymer via Digital Volume Correlation", *Coupled Syst. Mech.*, **10**(6), 545-560. https://doi.org/10.12989/csm.2021.10.6.545ï.

Vrgoč, A., Tomičević, Z., Zaplatić, A. and Hild, F. (2021), "Damage analysis in glass fibre reinforced epoxy resin via digital image correlation", *Trans. FAMENA*, **45**(2), 1-12.

Wang, Y., Charbal, A., Dufour, J.E., Hild, F., Roux, S. and Vincent, L. (2020), "Hybrid multiview correlation for measuring and monitoring thermomechanical fatigue test", *Exp. Mech.*, **60**(1), 13-33. https://doi.org/10.1007/s11340-019-00500-8.

Wang, Y., Charbal, A., Hild, F., Roux, S. and Vincent, L. (2019), "Crack initiation and propagation under thermal fatigue of austenitic stainless steel", *Int. J. Fatig.*, **124**, 149-166. https://doi.org/10.1016/j.ijfatigue.2019.02.036.

Xavier, J., Oliveira, M., Morais, J. and Pinto, T. (2009), "Measurement of the shear properties of clear wood by the Arcan test", *Holzforschung*, **63**(2), 217-225. https://doi.org/10.1515/HF.2009.034.

Zaplatić, A., Tomičević, Z., Čakmak, D. and Hild, F. (2022a), "Identifiability of Ludwik's law parameters depending on the sample geometry via inverse identification procedure", *Coupled Syst. Mech.*, **11**(2), 133-149. https://doi.org/10.12989/csm.2022.11.2.133.

Zaplatić, A., Tomičević, Z., Čakmak, D. and Hild, F. (2022b), "Improvement of the Arcan setup for the investigation of thin sheet behavior under shear loading", *Exp. Mech.*, **62**(2), 313-332. https://doi.org/10.1007/s11340-021-00762-1.

Zaplatić, A., Vrgoč, A., Tomičević, Z. and Hild, F. (2023), "Boundary condition effect on the evaluation of stress triaxiality fields", *Int. J. Mech. Sci.*, **246**, 108127. https://doi.org/10.1016/j.ijmecsci.2023.108127.